

Chandra observations of RXJ1347.5-1145: the distribution of mass in the most X-ray luminous galaxy cluster known

S.W. Allen, R.W. Schmidt and A.C. Fabian

Institute of Astronomy, Madingley Road, Cambridge CB3 0HA

November 3, 2018

ABSTRACT

We present Chandra observations of RXJ1347.5-1145, the most X-ray luminous cluster of galaxies known. We report the discovery of a region of relatively hot, bright X-ray emission, located approximately 20 arcsec to the southeast of the main X-ray peak, at a position consistent with the region of enhanced Sunyaev-Zeldovich effect reported by Komatsu *et al.* (2001). We suggest that this region contains shocked gas resulting from a recent subcluster merger event. Excluding the data for the southeast quadrant, the cluster appears relatively relaxed. The X-ray gas temperature rises from $kT \sim 6$ keV within the central $25 h_{50}^{-1}$ kpc radius to a mean value of ~ 16 keV between $0.1 - 0.5 h_{50}^{-1}$ Mpc. The mass profile for the relaxed regions of the cluster, determined under the assumption of hydrostatic equilibrium, can be parameterized by a Navarro, Frenk & White (1997) model with a scale radius $r_s \sim 0.4 h_{50}^{-1}$ Mpc and a concentration parameter $c \sim 6$. The best-fit Chandra mass model is in good agreement with independent measurements from weak gravitational lensing studies. Strong lensing data for the central regions of the cluster can be also explained by the introduction of an additional mass clump centred on the second brightest galaxy. We argue that this galaxy is likely to have been the dominant galaxy of the recently merged subcluster.

Key words: galaxies: clusters: individual: RXJ1347.5-1145 – gravitational lensing – X-rays: galaxies – cooling flows – intergalactic medium

1 INTRODUCTION

The launch of the Chandra Observatory (Weisskopf *et al.* 2000) in 1999 July has provided the first opportunity for detailed, spatially-resolved X-ray spectroscopy of clusters of galaxies at moderate to high redshifts. The Advanced CCD Imaging Spectrometer (ACIS) on Chandra permits direct, simultaneous measurements of the X-ray gas temperature and density profiles in clusters and, via the hydrostatic assumption, the mass distributions, spanning scales from $r \sim 10$ kpc in cluster cores out to $r \sim 1$ Mpc at the detection limits.

In this paper, we present the first results from Chandra observations of RXJ1347.5-1145, the most X-ray luminous galaxy cluster known (Schindler *et al.* 1995). This cluster has been the subject of several previous X-ray, optical and Sunyaev-Zeldovich (SZ) effect studies (*e.g.* Schindler *et al.* 1995, 1997; Fischer & Tyson 1997, Allen 1998; Komatsu *et al.* 1999, 2001; Pointecouteau *et al.* 1999, 2001). Here, we present the first measurements of the X-ray temperature structure within the cluster and place tight constraints on the total mass distribution. We compare our results with those from strong and weak lensing analyses. A comparison of the Chandra and SZ results, and a determination of the

Hubble Constant from the combined data sets, is presented elsewhere (Schmidt & Allen 2002, in preparation).

Except where stated otherwise, the cosmological parameters $H_0=50$ km s $^{-1}$ Mpc $^{-1}$, $\Omega = 1$ and $\Lambda = 0$ are assumed. At the redshift of RXJ1347.5-1145 ($z = 0.451$), an angular scale of 1 arcsec corresponds to physical size of 6.81 kpc in this cosmology.

2 OBSERVATIONS

The Chandra observations of RXJ1347.5-1145 were carried out using the ACIS on 2000 March 05 and 2000 April 29. The target was observed in the back-illuminated S3 detector and positioned near the centre of node-1 on CCD 7. The light curves for both observations were of high quality with no strong background flares. The net good exposure times were 8.9 and 10.0 ks, respectively, giving a total good exposure time of 18.9 ks. The focal plane temperature at the time of both observations was ~ 120 C.

We have used the CIAO software and the level-2 events files provided by the standard Chandra pipeline processing for our analysis. Only those X-ray events with grade classi-

arXiv:astro-ph/0111368v2 4 Apr 2002

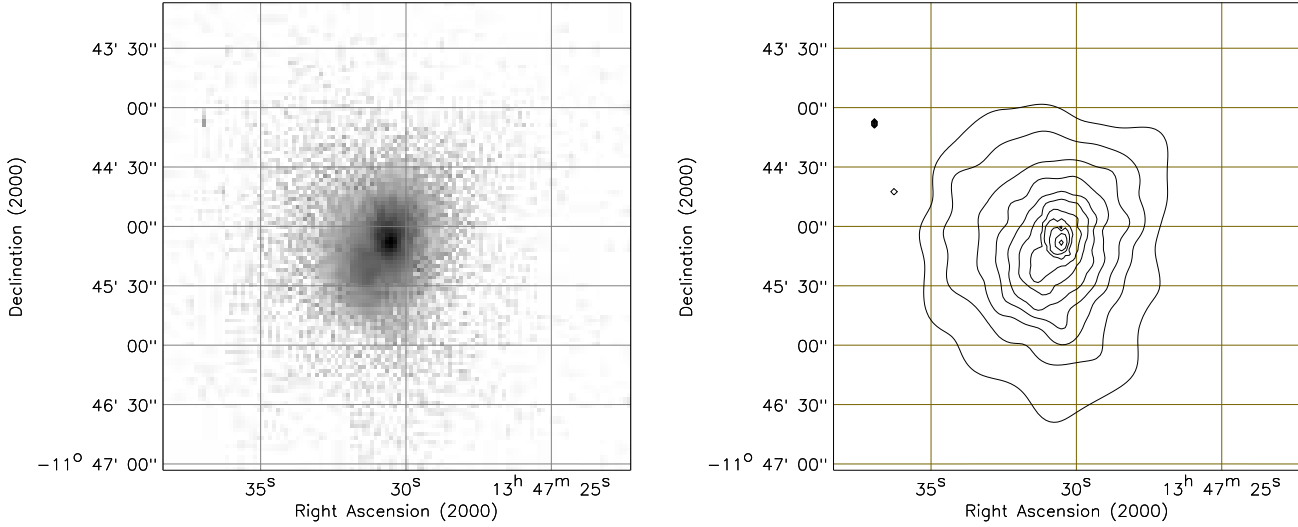


Figure 1. (a) The raw 0.3 – 7.0 keV Chandra image of RXJ1347.5-1145. The pixel size is 4 detector pixels (1.97 arcsec). (b) Contour plot of the same region, adaptively smoothed using the code of Ebeling *et al.* (2002) with a threshold value of 3σ . The contours have equal logarithmic spacing.

fications of 0,2,3,4 and 6 were included in our final cleaned data sets.

3 X-RAY IMAGING

3.1 X-ray morphology

The raw 0.3 – 7.0 keV image of the central 6×6 arcmin² region of the cluster, from the combined 18.9 ks data set, is shown in Fig. 1(a). The pixel size is 1.97×1.97 arcsec², corresponding to 4×4 raw detector pixels. Fig. 1(b) shows an adaptively smoothed contour plot of the same data, using the smoothing algorithm of Ebeling, White & Rangarajan (2002). The images reveal a number of notable features. Firstly, we see a sharp central surface brightness peak at a position 13h47m30.63 -11d45m09.3s (J2000.), in good agreement with the optical centroid for the dominant cluster galaxy, 13h47m30.5 -11d45m09s (J2000.; Schindler *et al.* 1995). Secondly, we identify a region of enhanced emission ~ 20 arcsec to the southeast of the X-ray peak (see below). Thirdly, on large scales ($r \sim 80$ arcsec) we detect an extension of the X-ray isophotes to the south.

Fig. 2 shows the data for the central regions of the cluster on a finer 0.492×0.492 arcsec² scale (corresponding to 1×1 raw detector pixels). From this figure it appears that the region of enhanced emission to the southeast of the X-ray peak has a roughly circular morphology with a flattened northwest edge. Beyond this edge, at a radius $r \sim 10$ arcsec, the X-ray subclump appears to be separated from the main cluster core by a valley of reduced emission. The spectral analysis in Section 4.2 shows that the X-ray subclump has a hotter temperature than the gas at the same radius in other directions from the X-ray peak and probably contains shocked gas resulting from a recent subcluster merger event.

Komatsu *et al.* (2001) report the detection of a region of enhanced SZ effect at a position coincident with the X-ray subclump. The enhanced SZ effect is consistent with the higher temperature and density for this region measured from the Chandra data.

No strong X-ray point sources are detected in the Chandra S3 field. (The brightest point source has a flux of 3.1×10^{-14} erg cm⁻² s⁻¹ in the 0.5 – 7.0 keV band; Gandhi *et al.*, in preparation.)

3.2 Surface brightness profiles

The azimuthally-averaged, 0.3 – 7.0 keV X-ray surface brightness profile for RXJ1347.5-1145 for position angles of 180 – 90 degrees (i.e. excluding the southeast quadrant) and for the disturbed, southeast quadrant are shown in Figs. 3(a,b), respectively. The profiles have been flat-fielded and background subtracted using an on-chip region free from cluster emission. The bin-size is 2 detector pixels (0.984 arcsec).

We see that the data for position angles of 180 – 90 degrees appear regular and, for $r < 500$ kpc, can be approximated ($\chi^2 = 102$ for 72 degrees of freedom) by a β -model (e.g. Jones & Forman 1984) of the form $S_X(r) = S(0) [1 + (r/r_c)^2]^{1/2-3\beta}$ with a core radius $r_c = 29.2 \pm 0.7$ kpc and a slope parameter $\beta = 0.535 \pm 0.003$ (1σ errors). Between radii of 0.1 – 1.0 Mpc we find evidence for a steepening of the surface brightness profile with increasing radius: for $0.1 < r < 1.0$ Mpc the data can be described ($\chi^2 = 135$ for 131 degrees of freedom) by a simple broken power-law model, with a break at a radius of 487_{-16}^{+23} kpc, and slopes in the regions internal and external to the break radius of -2.25 ± 0.03 and -3.66 ± 0.18 , respectively. A similar result was obtained for Abell 2390 by Allen, Ettori & Fabian

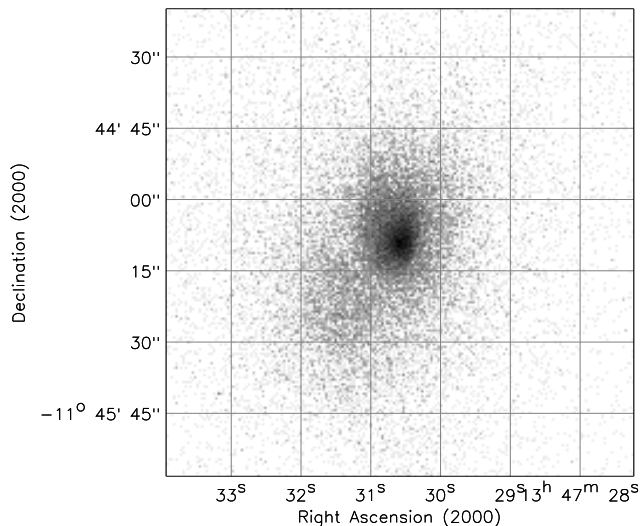


Figure 2. A raw 0.3 – 7.0 keV image of the central regions of RXJ1347.5-1145 on a finer spatial scale (pixel size 0.492×0.492 arcsec², equivalent to 1×1 raw detector pixels).

(2001b), although in that case the slope interior to the break radius was flatter.

The data for the southeast quadrant containing the X-ray subclump reveal a clear excess of emission relative to other directions. Enhanced emission is detected between radii of $\sim 70 - 300$ kpc, with a maximum enhancement of a factor ~ 3 at a radius $r \sim 180$ kpc.

4 SPATIALLY-RESOLVED SPECTROSCOPY

4.1 Method

For our spectral analysis, we have separated the southeast quadrant containing the X-ray subclump from the rest of the cluster. The data for position angles of $180 - 90$ (the relaxed part of the cluster) were divided into the annular regions detailed in Table 1.* A single spectrum was extracted for each region in 1024 Pulse Invariant (PI) channels. The spectra were re-grouped to contain a minimum of 20 counts per PI channel thereby allowing χ^2 statistics to be used.

Background spectra, appropriate for the regions studied, were extracted from the ACIS-S3 blank-field data sets provided by Maxim Markevitch (which are available from the Chandra X-ray Center). Separate photon-weighted response matrices and effective area files were constructed for each region using the available calibration and response files appropriate for the -120C focal plane temperature.†

* For the southeast quadrant, we have extracted a single spectrum covering radii 60–195 kpc (18-58 pixels), where the emission enhancement in Fig. 2 is most obvious.

† For each 32×32 pixel² sub-region of the S3 chip, a spectral response (.rmf) and an auxiliary response (.arf) matrix were created using the CIAO tools *mkrmf* and *mkarf*, respectively. For

Table 1. The results from the analysis of the annular spectra (covering position angles $180 - 90$ degrees). Temperatures (kT) are in keV and metallicities (Z) in solar units. The absorbing column density has been fixed at the nominal Galactic value of 4.85×10^{20} atom cm⁻². The total χ^2 values and number of degrees of freedom (DOF) in the fits are listed in column 4. Error bars are the 1σ ($\Delta\chi^2 = 1.0$) confidence limits on a single interesting parameter.

Radius (kpc)	kT	Z	χ^2/DOF
0 – 23.5	$7.04^{+0.79}_{-0.60}$	$0.48^{+0.17}_{-0.17}$	127.6/101
23.5 – 50.3	$9.03^{+0.99}_{-0.74}$	$0.66^{+0.16}_{-0.15}$	126.4/130
50.3 – 97.2	$11.23^{+1.22}_{-1.02}$	$0.60^{+0.16}_{-0.15}$	190.6/164
97.2 – 147	$13.82^{+2.09}_{-1.69}$	$0.07^{+0.17}_{-0.07}$	106.3/119
147 – 245	$19.37^{+4.07}_{-2.83}$	$0.28^{+0.26}_{-0.26}$	134.7/134
245 – 345	$13.51^{+2.73}_{-2.11}$	$0.81^{+0.34}_{-0.30}$	78.2/89
345 – 492	$18.08^{+5.84}_{-4.23}$	$0.79^{+0.47}_{-0.42}$	92.6/85
492 – 737	$12.40^{+4.52}_{-2.61}$	$0.44^{+0.33}_{-0.35}$	80.2/81
0 – 97.2	$9.32^{+0.57}_{-0.52}$	$0.55^{+0.09}_{-0.09}$	457.9/399
97.2 – 737	$15.48^{+1.53}_{-1.16}$	$0.34^{+0.12}_{-0.12}$	502.7/516
0 – 737	$12.00^{+0.62}_{-0.59}$	$0.41^{+0.07}_{-0.07}$	987.8/917

The data from both Chandra observations were modelled simultaneously using the XSPEC code (version 11.01; Arnaud 1996). We have limited our analysis to the 0.5 – 7.0 keV energy band, over which the calibration of the back-illuminated CCD detectors is currently best understood.

The spectra have been modelled using the MEKAL plasma emission code of Kaastra & Mewe (1993; incorporating the Fe L calculations of Liedhal, Osterheld & Goldstein 1995) and the photoelectric absorption models of Balucinska-Church & McCammon (1992). We have fitted each annular spectrum using a simple, single-temperature model with the absorbing column density fixed at the nominal Galactic value ($N_{\text{H}} = 4.85 \times 10^{20}$ atom cm⁻²; Dickey & Lockman 1990). The free parameters in this model were the temperature (kT), metallicity (Z ; measured relative to the solar photospheric values of Anders & Grevesse 1989, with the various elements assumed to be present in their solar ratios) and emission measure. We note that including the absorbing column density as an additional free parameter did not result in significant improvements in the goodness of fit.

4.2 Results

The best-fit parameter values and 1σ ($\Delta\chi^2 = 1.0$) confidence limits determined from the fits to the annular spectra (excluding the southeast quadrant) in the 0.5 – 7.0 keV band are summarized in Table 1. The projected temperature

each of the annular regions studied, the number of source counts in each 32×32 pixel² sub-region was determined. The individual .rmf and .arf files were then combined using the FTOOLS programs *addrmf* and *addarf* (using a script provided by Roderrick Johnstone) to form a counts-weighted spectral response and auxiliary response matrix appropriate for each annulus.

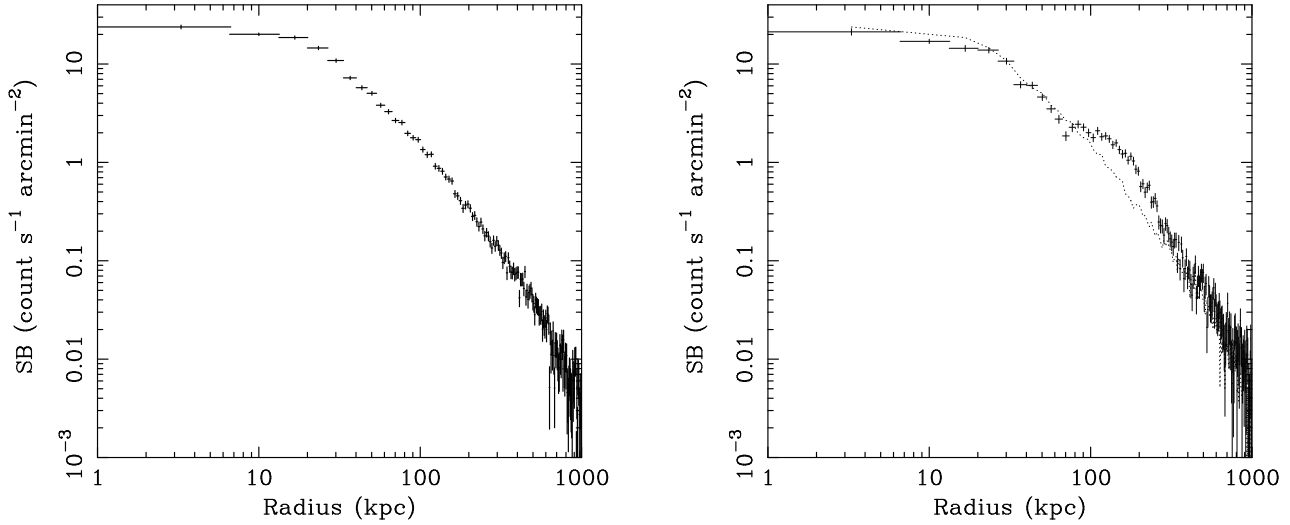


Figure 3. Background-subtracted, flat-fielded, azimuthally-averaged radial surface brightness profiles for RXJ1347.5-1145 in the 0.3–7.0 keV band. The bin-size is 0.984 arcsec (6.70 kpc). (a) The results for position angles of 180–90 degrees. The profile appears regular and relaxed (b) The results for position angles of 90–180 degrees (the southeast quadrant). The dotted curve shows the results for the 180–90 degree region. Note the clear excess of emission in the southeast quadrant between radii of 10–45 arcsec (70–300 kpc).

profile determined with this model is shown in Fig. 4. The temperature rises from a mean value of $7.0^{+0.8}_{-0.6}$ keV within $r = 24$ kpc to $kT = 15.8^{+1.6}_{-1.2}$ keV over the 0.1–0.5 Mpc region.

A fit with the same model to the data for the southeast quadrant between radii of 60–195 kpc (where the X-ray enhancement is most obvious in the image) gives a best-fit temperature $kT = 18.0^{+2.7}_{-2.3}$ keV. (A similar result, $kT = 18.2^{+3.8}_{-2.9}$ keV, is obtained using a circular region of radius 10 arcsec centred on the enhancement.) In other directions, the mean temperature between radii of 60–195 kpc is $kT = 12.7 \pm 1$ keV. The higher temperature and enhanced X-ray surface brightness in the southeast quadrant are consistent with the X-ray gas in that region having undergone shock compression (Section 8).

We find marginal evidence for a metallicity gradient in the cluster, with a mean metallicity for the central 100 kpc radius of $Z = 0.55 \pm 0.09$ solar, as opposed to $Z = 0.34 \pm 0.12$ solar for the 100–740 kpc region.

4.3 Spectral deprojection analysis

The results discussed above are based on the analysis of projected spectra. We have also carried out a simple deprojection analysis of the Chandra spectral data using the method described by Allen *et al.* (2001b).

For this analysis we have used the same annular regions (covering position angles of 180–90 degrees) and have assumed that the emission from each spherical shell (the shells are defined by the same inner and outer radii as the annular regions) is isothermal and absorbed by the Galactic column density. The fit to the outermost annulus is used to determine the temperature and emission measure in the outermost spherical shell. The contribution from that shell to each inner annulus is then determined by purely geometric factors (*e.g.* Kriss, Cioffi & Canizares 1983). The fit to the

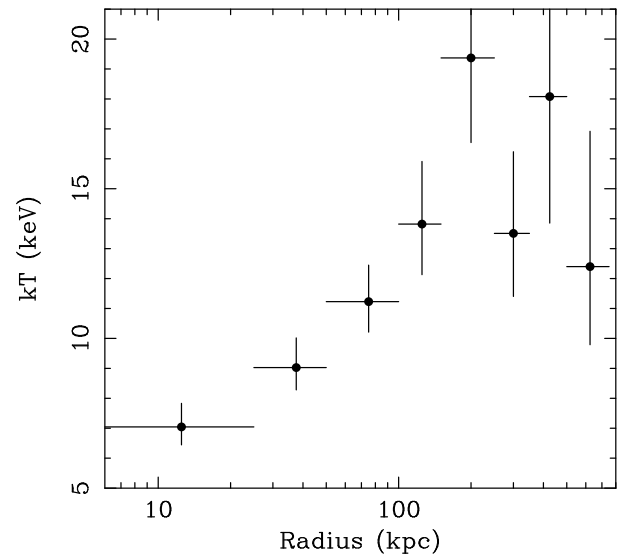


Figure 4. The projected X-ray gas temperature profile (and 1 σ errors) measured from the Chandra data in the 0.5–7.0 keV energy band.

second annulus inward is used to determine the parameters for the second spherical shell, and so forth, working inwards.

The data for all eight annular spectra were fitted simultaneously in order to determine the parameter values and confidence limits. The metallicity was linked to take the same value at all radii. The temperature profile determined with the spectral deprojection method is shown in Fig. 5.

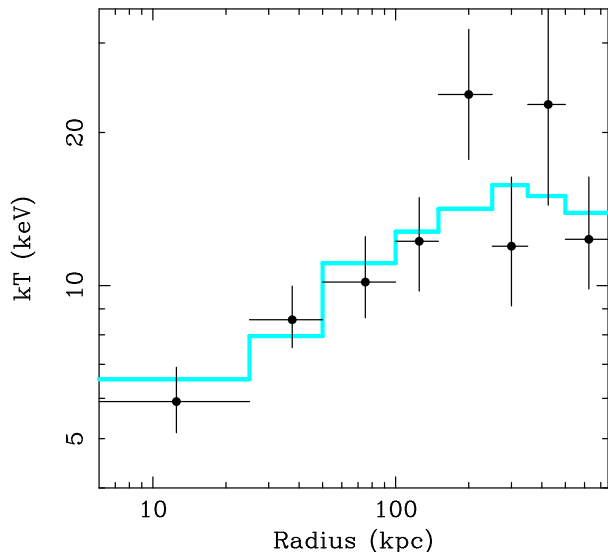


Figure 5. The predicted deprojected temperature profile (grey curve) determined from 100 Monte-Carlo simulations using the best-fitting NFW mass model (with $r_s = 0.40$ Mpc, $c = 5.87$ and $\sigma = 1450$ km s $^{-1}$; Section 5). The predicted profile has been binned to the same spatial resolution as the spectral deprojection results (solid points; Section 4.3), which have been overlaid. The agreement between the deprojected spectral results and the best-fit NFW mass model predictions (reduced $\chi^2_\nu = 0.87$ for $\nu = 6$ degrees of freedom) indicates that the NFW mass model provides a good description of the spatially-resolved Chandra spectra.

4.4 Comparison with previous work

The mean emission-weighted temperature and metallicity for RXJ1347.5-1145 of $kT = 12.2 \pm 0.6$ keV and $Z = 0.42 \pm 0.07$ solar, respectively, measured in the 0.0 – 0.74 Mpc range over the full 360 degrees, are in good agreement with the values reported by Allen & Fabian (1998; $kT = 12.5^{+0.9}_{-0.8}$ keV, $Z = 0.38^{+0.11}_{-0.10}$ solar) using ASCA data and a similar spectral model. Excluding the data for the southeast quadrant, we obtain only small changes in these results: $kT = 12.0 \pm 0.6$ keV and $Z = 0.41 \pm 0.07$ solar. The Chandra results are also in good agreement with those reported by Schindler *et al.* (1997) using the same ASCA data and a 3 arcmin radius aperture ($kT = 11.8^{+1.6}_{-1.0}$ keV, $Z = 0.39^{+0.12}_{-0.13}$ solar). The emission-weighted temperature measured with Chandra is slightly cooler than the value of $14.5^{+1.7}_{-1.5}$ keV measured with BeppoSAX by Ettori, Allen & Fabian (2001), as can be expected given the observed temperature profile (Figs. 4,5) and the different response characteristics of the instruments. (The data for the southeast quadrant are not excluded from the BeppoSAX or ASCA studies.)

The ‘ambient’ emission-weighted temperature measured with Chandra in the 0.1 – 0.5 Mpc range (*i.e.* excluding the data for the southeast quadrant, the central, cool region, and the regions at large radii where the temperature may start to decline again) of $kT = 15.8^{+1.6}_{-1.2}$ keV is in good agreement with the value of $15.9^{+6.5}_{-2.6}$ keV estimated from BeppoSAX data by Ettori *et al.* (2001) using a spectral model which included a constant-pressure cooling flow component. The Chandra result is also consistent with the ambient temper-

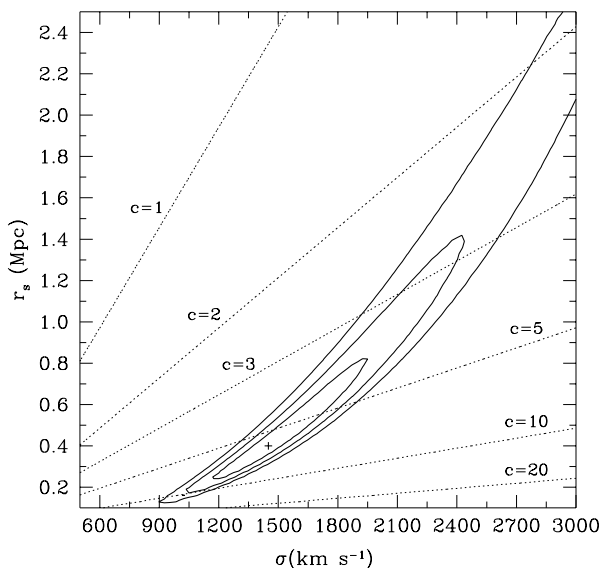


Figure 6. Contour plot showing the 68.3% (1σ), 95.4% (2σ) and 99.73% (3σ) confidence contours on the scale radius, r_s , and the effective velocity dispersion, σ , for the NFW mass models. Contours of constant concentration parameter, c , are marked with dashed lines. The best-fit model is marked by a plus sign.

ature of $kT = 26^{+8}_{-12}$ keV estimated from ASCA data using a similar constant-pressure cooling flow model (Allen & Fabian 1998), and $kT = 18.6^{+4.1}_{-3.0}$ keV from a re-analysis of the ASCA data by the same authors using the more appropriate ‘isothermal’ cooling flow models of Nulsen (1998).

The emission weighted ambient temperature determined from the Chandra data in the 0.1 – 0.5 Mpc region is in good agreement with the mean gas mass-weighted temperature of $16.1^{+5.3}_{-2.7}$ keV measured within r_{2500} ($r = 0.72$ Mpc) by Allen, Schmidt & Fabian (2001c). We note that this temperature is also consistent with the predicted value of $kT = 16.8$ keV, using the cooling-flow corrected kT_X/L_{Bol} relation of Allen & Fabian (1998; we assume a bolometric luminosity of $\sim 2.2 \times 10^{46}$ erg s $^{-1}$ as measured by ASCA).

5 MEASUREMENT OF THE CLUSTER MASS PROFILE

5.1 Method

The observed X-ray surface brightness profile (Fig. 3a) and deprojected, spectrally-determined temperature profile (Fig. 5) may together be used to determine the X-ray gas mass and total mass profiles in the cluster. For this analysis, we have used an enhanced version of the image deprojection code described by White, Jones & Forman (1997), and have followed the methods outlined by Allen *et al.* (2001b) and Schmidt *et al.* (2001).

A variety of simple parameterizations for the cluster mass distribution were examined to establish which could provide an adequate description of the Chandra data (see below). The best-fit parameter values and confidence limits

were determined by examining parameter grids and evaluating χ^2 for each set of parameters.[‡] Spherical symmetry and hydrostatic equilibrium are assumed throughout.

5.2 NFW mass models

We find that a good fit ($\chi_{\min}^2 = 5.2$ for 6 degrees of freedom, hereafter DOF) to the Chandra data for RXJ1347.5-1145 can be obtained using a Navarro, Frenk & White (1997, hereafter NFW) model:

$$\rho(r) = \frac{\rho_{\text{crit}}(z)\delta_c}{(r/r_s)(1+r/r_s)^2}, \quad (1)$$

where $\rho(r)$ is the mass density, $\rho_{\text{crit}}(z) = 3H(z)^2/8\pi G$ is the critical density for closure and

$$\delta_c = \frac{200}{3} \frac{c^3}{[\ln(1+c) - c/(1+c)]}. \quad (2)$$

The best-fit scale radius, $r_s = 0.40^{+0.24}_{-0.12}$ Mpc and the concentration parameter, $c = 5.87^{+1.35}_{-1.44}$ (68 per cent confidence limits). The normalization of the mass profile may also be expressed in terms of an effective velocity dispersion, $\sigma = \sqrt{50}H(z)r_sc = 1450^{+300}_{-200}$ km s⁻¹ (with r_s in units of Mpc). The deprojected X-ray gas temperature profile predicted by the best-fitting NFW mass model (given the observed surface brightness profile) is shown overlaid on the observed spectral results in Fig. 5.

Fig. 6 shows a contour plot of the χ^2 values obtained for the full range of NFW models studied. The minimum χ^2 value is marked with a cross. Contours have been drawn at intervals of $\Delta\chi^2 = 2.30, 6.17$ and 11.8 , corresponding to formal confidence limits of 68.3 (1 σ), 95.4 (2 σ) and 99.73 (3 σ) per cent for two interesting parameters. Fig. 7 shows the best-fitting NFW mass profile, which has a virial radius $r_{200} = cr_s = 2.35^{+0.49}_{-0.33}$ Mpc and an integrated mass within the virial radius, $M_{200} = 2.29^{+1.74}_{-0.82} \times 10^{15} M_{\odot}$.

5.3 Other parameterized mass models

We have also examined a variety of other popular parameterized mass models. Firstly, the model of Moore *et al.* (1998):

$$\rho(r) = \frac{\rho_{\text{crit}}(z)\delta_{\text{cm}}}{(r/r_s)^{1.5}(1+r/r_s)^{1.5}}, \quad (3)$$

where

[‡] The observed surface brightness profile (Fig. 3a) and a particular parameterized mass model are together used to predict the temperature profile of the X-ray gas. (We use the median temperature profile determined from 100 Monte-Carlo simulations in which the surface brightness profile is perturbed according to the statistical uncertainties at each radius. The outermost pressure is fixed using an iterative technique which ensures a smooth pressure gradient in these regions.) The predicted temperature profile is rebinned to the same binning as the spectral results and the χ^2 difference between the observed and predicted, deprojected temperature profiles is calculated. The parameters for the mass model are stepped through a regular grid of values in the r_s - σ plane (see text) to determine the best-fit values and 68 per cent confidence limits. The gas mass profile is determined to high precision at each grid point using the observed surface brightness profile and model temperature profile.

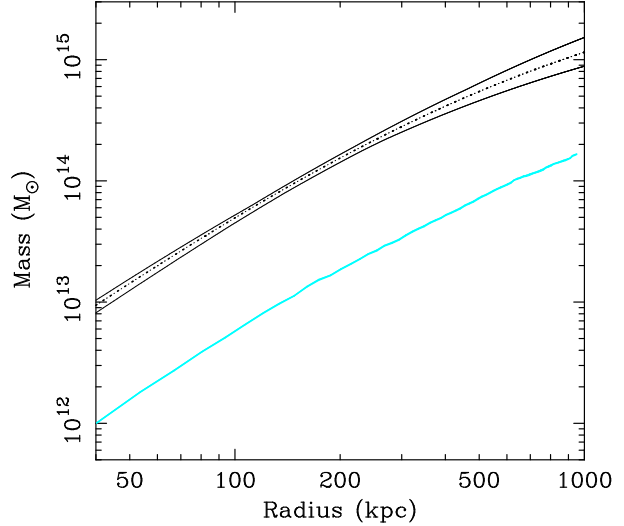


Figure 7. The integrated (3-dimensional) mass profile and 1 σ errors for RXJ1347.5-1145 determined from the Chandra data using the NFW parameterization (section 5.2). The grey curve shows the X-ray gas mass profile. (The best-fit X-ray gas mass profile and 1 σ errors are plotted, although these curves are indistinguishable in the figure.)

$$\delta_{\text{cm}} = 100 \frac{c_m^3}{\ln(1+c_m^{1.5})}. \quad (4)$$

For this model we obtain $\chi_{\min}^2 = 8.6$ (6 DOF), with best-fit values for the scale radius $r_s = 5.0$ Mpc (the maximum allowed value in our grid), concentration parameter $c_m = 0.69$ and effective velocity dispersion $\sigma = 2125$ km s⁻¹ (where $\sigma = \sqrt{50}H_0(z)r_sc_m$).

Secondly, we examined a simple, non-singular isothermal sphere model:

$$\rho(r) = \frac{\sigma_{\text{iso}}^2}{2\pi G} \frac{1}{r^2 + r_c^2}, \quad (5)$$

for which we obtain $\chi_{\min}^2 = 4.9$ (6 DOF) with $r_c = 45 \pm 10$ kpc and $\sigma_{\text{iso}} = 1590 \pm 150$ km s⁻¹.

We thus find that all of the two-parameter mass models described above provide acceptable descriptions of the Chandra data for RXJ1347.5-1145. We note, however, that a singular isothermal sphere [$\rho(r) \propto r^{-2}$] does not provide an acceptable fit ($\chi_{\min}^2 = 33.1$ for 7 DOF).

6 COMPARISON WITH GRAVITATIONAL LENSING RESULTS

6.1 Weak lensing

Fischer & Tyson (1997) present a detailed weak lensing study of RXJ1347.5-1145. They measure a mass profile that can be parameterized by an NFW model with $r_{200} = 2.4$ Mpc, or a singular isothermal sphere with $\sigma = 1500$ km s⁻¹, in good agreement with the Chandra results.

The azimuthally-averaged, projected surface mass density profile for RXJ1347.5-1145 determined by Fischer & Tyson (1997) is shown in Fig. 8. We have excluded the innermost point from their data, which extends into the strong

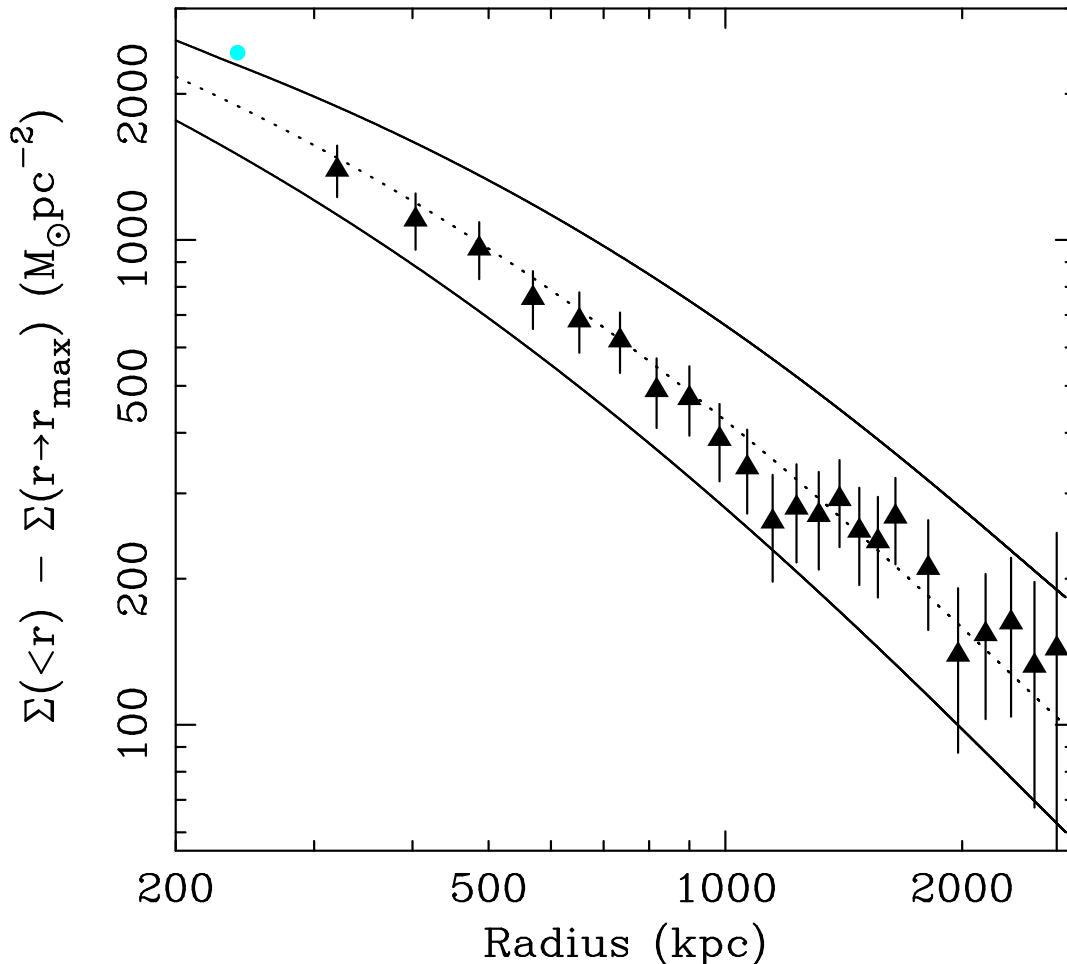


Figure 8. A comparison of the projected surface mass density contrast determined from the Chandra X-ray data (Section 5) with the weak lensing results of Fischer & Tyson (1997; solid triangles) and the strong lensing result from Section 6.2 (grey circle). The best-fit NFW X-ray mass model for the relaxed regions of the cluster and 1σ confidence limits (the maximum and minimum values at each radius for all NFW models within the 68 per cent confidence contour shown in Fig. 6) are shown as the dotted and full curves, respectively. The strong lensing point is marked with a grey circle. Note that the strong lensing point should lie above the X-ray results, which exclude the regions of the cluster affected by the second mass clump. We adopt $r_{\max} = 2.72$ Mpc as in Fischer & Tyson (1997).

lensing regime (see below; $r_{\max} = 2.72$ Mpc in our adopted cosmology). The same quantity, calculated for all NFW mass models within the 68 per cent confidence contour determined from the Chandra X-ray data (Fig. 6) has been overlaid. We see that the Chandra and weak-lensing results exhibit good agreement on all spatial scales studied.

The agreement between the independent lensing and X-ray mass measurements confirms the validity of the hydrostatic assumption used in the X-ray analysis (having excluded the southeast quadrant) and suggests that the mass profile in the cluster has been robustly determined.

6.2 Strong lensing

Schindler *et al.* (1995) report the discovery of two bright gravitationally-lensed arcs in RXJ1347.5-1145 using ground based optical imaging. Sahu *et al.* (1998) present Hubble Space Telescope Imaging Spectrograph (STIS) observations of the cluster which reveal a number of additional strongly-

lensed features. The STIS image for RXJ1347.5-1145 is shown in the left panel of Fig. 9. Sahu *et al.* (1998) also present ground-based spectroscopy of the bright northern arc in the cluster (arc 1) at a radius of 34.9 arcsec (240 kpc) from the dominant cluster galaxy, for which they measure a redshift $z_1 = 0.806$.

Following the methods outlined in Schmidt *et al.* (2001), we have examined the constraints that the observed strong lensing configuration can place on the mass distribution in the cluster core. We first examined a simple, spherically-symmetric mass model, centred on the dominant cluster galaxy, with the best-fit parameter values determined from the Chandra data for the relaxed regions of the cluster (Sect. 5.2). We find that such a mass model does not provide a sufficient central mass density to explain the strong lensing data.

We next examined refined lensing models in which a second mass component, centered on the second brightest galaxy was introduced, together with appropriate elliptici-

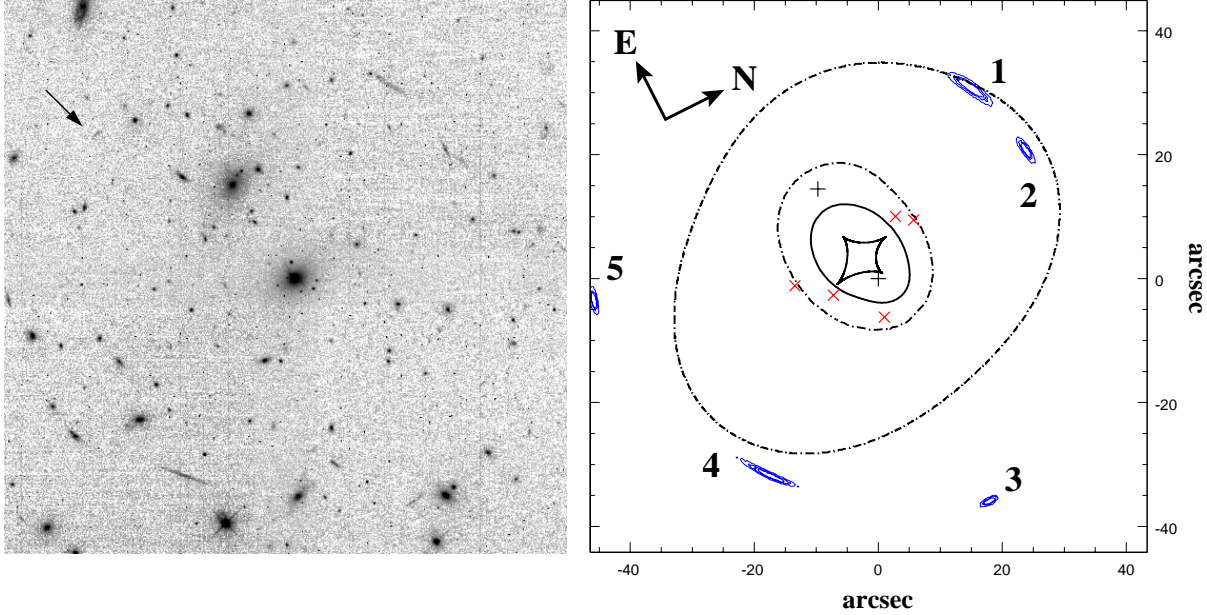


Figure 9. The (a) observed and (b) predicted gravitational arc geometry in RXJ1347.5-1145. The image in the left panel has been compiled from archival HST STIS data that were originally presented by Sahu *et al.* (1998). The arrow points to an additional arc-like feature mentioned in the text. The right panel shows the arc geometry predicted by our two-component mass model. The arc numbering has been taken from Sahu *et al.* (1998). The arcs have been simulated using circular Gaussian surface brightness distributions. The 10%, 30% and 50% brightness contours are plotted. The true source positions are denoted by crosses, with details in Table 2. The central positions for the two mass components are marked with plus signs. Also shown are the critical curves (dash-dotted) and caustic lines (solid; e.g., Schneider, Ehlers & Falco 1992) for a source at a redshift of $z = 0.97$.

ties for the matter distributions. (The introduction of such a mass clump is well-motivated by the Chandra data for the southeast quadrant of the cluster. The second brightest galaxy is likely to have been the dominant galaxy of the recently-merged subcluster; Section 8). Both mass components have been modelled by elliptical NFW models (see Schmidt *et al.* 2001 for definitions). The parameters for the main mass component were fixed to the values determined from the Chandra data for the relaxed regions of the cluster in Sect. 5.2, *i.e.* scale radius $r_s = 0.4$ Mpc, velocity dispersion $\sigma = 1450 \text{ km s}^{-1}$ and concentration parameter $c = 5.87$. The axis ratio and position angle were fixed to the values measured for the dominant galaxy from the STIS data: axis ratio $q = 0.76$ and position angle $\theta = 13.1^\circ$. The centre of the main mass component was fixed to the centre of the dominant galaxy.

The parameters for the second mass component have been determined by requiring that the overall potential is able to produce the northern arc (arc 1) at the measured redshift, $z_1 = 0.806$. For an assumed scale radius $r_{s,\text{clump}} = 0.25$ Mpc, we obtain a best-fitting velocity dispersion $\sigma_{\text{clump}} = 815 \text{ km s}^{-1}$ and a concentration parameter $c_{\text{clump}} = 5.3$. Such parameters are typical for mid-temperature galaxy clusters ($kT \sim 5$ keV, *e.g.* Allen *et al.* 2001c). The position, ellipticity and position angle of the second mass component were fixed to the values determined for the second brightest galaxy from the STIS image: $q_{\text{clump}} = 0.79$ and $\theta_{\text{clump}} = 28.1^\circ$.

The redshift measurement for the northern arc constrains the projected mass within the arc radius. It is possi-

Table 2. The redshifts, sizes (in arcsec) and positions (offsets in arcsec with respect to the dominant cluster galaxy in the STIS reference frame) for the sources in the lens model shown in Fig. 9.

arc	redshift	size (FWHM)	position Δx Δy	
1	0.806	0.8	2.77	10.03
2	0.75	0.6	5.71	9.44
3	0.97	0.6	1.00	-6.23
4	0.97	0.5	-7.24	-2.66
5	0.97	0.6	-13.44	-1.16

ble to vary the scale radius for the second mass component and to adjust the concentration parameter accordingly, so long as the projected mass within the arc radius remains constant. The absence of multiple arc images within the cluster core suggests $r_{s,\text{clump}} > 0.1$ Mpc.

Having adjusted the parameters for the second mass component to produce the northern arc, we then examined whether the resulting mass model can explain the other arcs observed by Sahu *et al.* (1998). Unfortunately, there are no measured redshifts for the other arcs. (Sahu *et al.* 1998 note a possible lower limit for arc 4 of $z \geq 1$ based on the non-detection of [OII] in their ground-based spectra, although they caution that the arc may simply be a galaxy without a strong emission-line feature). The details of our model predictions are shown in the right panel of Fig. 9. The results on the predicted arc redshifts and the assumed sizes of the sources are listed in Table 2. The predicted redshifts

are cosmology dependent and would be modified slightly if, for example, an accelerating universe with a different Hubble Constant were assumed. For the mass model used here, the predicted redshifts should be accurate to $\sim \pm 0.05$, with the exception of arc 4 which is determined more precisely. We have modelled the lensed galaxies using circular Gaussian brightness distributions with the full-width-at-half-maximum (FWHM) values listed in Table 2. The FWHMs for the arcs were adjusted so that their 30 per cent brightness contours provide a good fit to the STIS data. The effects of using different source sizes is illustrated by the different brightness contours in Fig. 9.

Although we include arc 2 in our modelling, we caution that this source appears quite red in the colour image published by Fischer & Tyson (1997) and that it is possible that the source is simply an edge-on spiral galaxy. The predicted redshift for arc 2 is lower than z_1 , since otherwise the lens model would predict a much stronger distortion. Arcs 3, 4 and 5 are consistent with being at the same redshift. The projected separation of the sources producing arcs 4 and 5 is $43.4 h_{50}^{-1}$ kpc. Although arcs 4 and 5 have a similar colour in the data of Fischer & Tyson (1997), it is not possible to explain them as images of the same source using our mass model. In exploring different redshifts for arc 3, we found that for redshifts higher than $z_3 \sim 1$ it is possible to produce a counter image on the other side of the central galaxy. This alerted us to the presence of a blue object (identified from the colour image of Fischer & Tyson 1997) to the south-east of the merging subclump (see the arrow in the left panel of Fig. 9). However, both the appearance in the STIS image and our lensing analysis suggest that these objects are not images of the same source.

We note that circular NFW models for one or both of the main mass components cannot explain the observed arc shapes and orientations well. In particular, the orientation of arc 4 reflects the orientation of the critical curve (Fig. 9) in its vicinity. A small $\sim 5^\circ$ difference between the orientation of the observed and predicted arc 4 remains in our best-fit model, which points to a small imprecision of the lensing model.

The grey circle in Fig. 8 shows the azimuthally-averaged, surface mass density contrast at $r = 240$ kpc (centred on the main mass component) for the best-fit strong lensing model. Note that the strong lensing results should lie above the X-ray results at the same radii, since the Chandra analysis excludes the regions of the cluster affected by the second mass subclump. The surface mass density contrast rises sharply between the innermost weak lensing point and the strong lensing result, suggesting that the second mass component is centrally concentrated and does not make a major contribution to the total mass beyond the strong lensing regime.

In conclusion we find that a simple two-component mass model, with ellipticities and orientations for the mass components matching those of the dominant cluster galaxies, provides a reasonable description for the overall arc geometry in RXJ1347.5-1145. Such a model is consistent with the Chandra X-ray and weak lensing results.

7 THE PROPERTIES OF THE CLUSTER GAS

7.1 Electron density and cooling time profiles

The results on the electron density and cooling time as a function of radius, determined from the image deprojection analysis using the best-fit NFW mass model, are shown in Fig. 10. Within the central 500 kpc radius, the electron density profile can be parameterized ($\chi^2 = 43.2$ for 34 degrees of freedom) by a β -profile with a core radius, $r_c = 27.8 \pm 1.6$ kpc, $\beta = 0.521 \pm 0.012$ and a central density, $n_e(0) = 2.3 \pm 0.1 \times 10^{-2} \text{ cm}^{-3}$ (1σ errors). We measure a central cooling time (*i.e.* the mean cooling time within the central 1.97 arcsec (~ 13.4 kpc) bin of $t_{\text{cool}} = 4.1_{-0.5}^{+0.6} \times 10^8$ yr (uncertainties are the 10 and 90 percentile values from 100 Monte Carlo simulations).

7.2 The X-ray gas mass fraction

The X-ray gas-to-total-mass ratio as a function of radius, $f_{\text{gas}}(r)$, determined from the Chandra data is shown in Fig. 11. We find that the best-fit f_{gas} value rises rapidly with increasing radius within the central $r \lesssim 40$ kpc radius and then remains approximately constant, or rises slowly, out to the limits of the data at $r = 0.74$ Mpc where we measure $f_{\text{gas}} = 0.141_{-0.027}^{+0.035}$.

Following the usual arguments, which assume that the properties of clusters provide a fair sample of those of the Universe as a whole (*e.g.* White & Frenk 1991; White *et al.* 1993; White & Fabian 1995; Evrard 1997; Ettori & Fabian 1999), we may use our results on the X-ray gas mass fraction to estimate the total matter density in the Universe, Ω_m . Assuming that the luminous baryonic mass in galaxies in RXJ1347-1145 is $0.134 h_{50}^{0.5}$ of the X-ray gas mass (*e.g.* White *et al.* 1993; Fukugita, Hogan & Peebles 1998) and neglecting other possible sources of baryonic dark matter in the cluster, one can show that $\Omega_m = \Omega_b/1.134 f_{\text{gas}}$, where Ω_b is mean baryon density in the Universe. For $\Omega_b h_{50}^2 = 0.0820 \pm 0.0072$ (O’Meara *et al.* 2001) we obtain $\Omega_m = 0.51 \pm 0.12$. For a Λ CDM cosmology with $H_0 = 70 \text{ km s}^{-1} \text{ Mpc}^{-1}$, our results for RXJ1347.5-1145 would imply $\Omega_m = 0.33 \pm 0.08$.

7.3 Cooling flow models

Under the assumption that the X-ray gas in the core of RXJ1347.5-1145 is in a steady-state cooling flow, we can parameterize the luminosity profile in terms of an equivalent mass deposition rate (*e.g.* White *et al.* 1997). The results of this calculation are shown in Fig. 12. We see that the integrated mass deposition rate (MDR) rises with increasing radius within the central 100 kpc, to a maximum value of $\sim 1300 M_\odot \text{ yr}^{-1}$.

We have examined the spectrum for the central 100 kpc (radius) region using a model appropriate for a cooling flow with distributed mass deposition. (We use the model of Nulsen 1998 and assume that the integrated MDR within radius r , $\dot{M} \propto r$.) The normalization of the cooling-flow component is parameterized in terms of a mass deposition rate, \dot{M} . The cooling flow was also allowed to be absorbed by an intrinsic column density, ΔN_H , of cold gas (with solar metallicity) located at the redshift of the cluster. Both \dot{M} and ΔN_H were free parameters in the fits. Accounting for projection effects, we find that the 0.5 – 7.0 keV spectrum

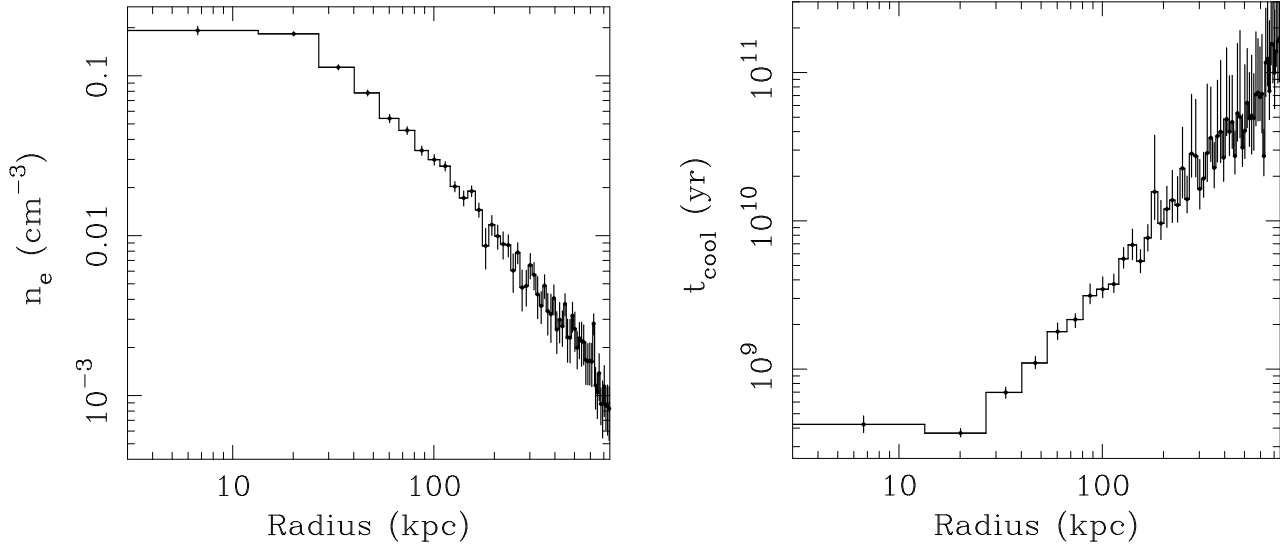


Figure 10. The results on (a) the electron density and (b) the cooling time, determined from the X-ray image deprojection analysis using the best-fit NFW mass model. Error bars are the 1σ errors determined from 100 Monte Carlo simulations. A Galactic column density of 4.85×10^{20} atom cm^{-2} and a metallicity of 0.4 solar are assumed.

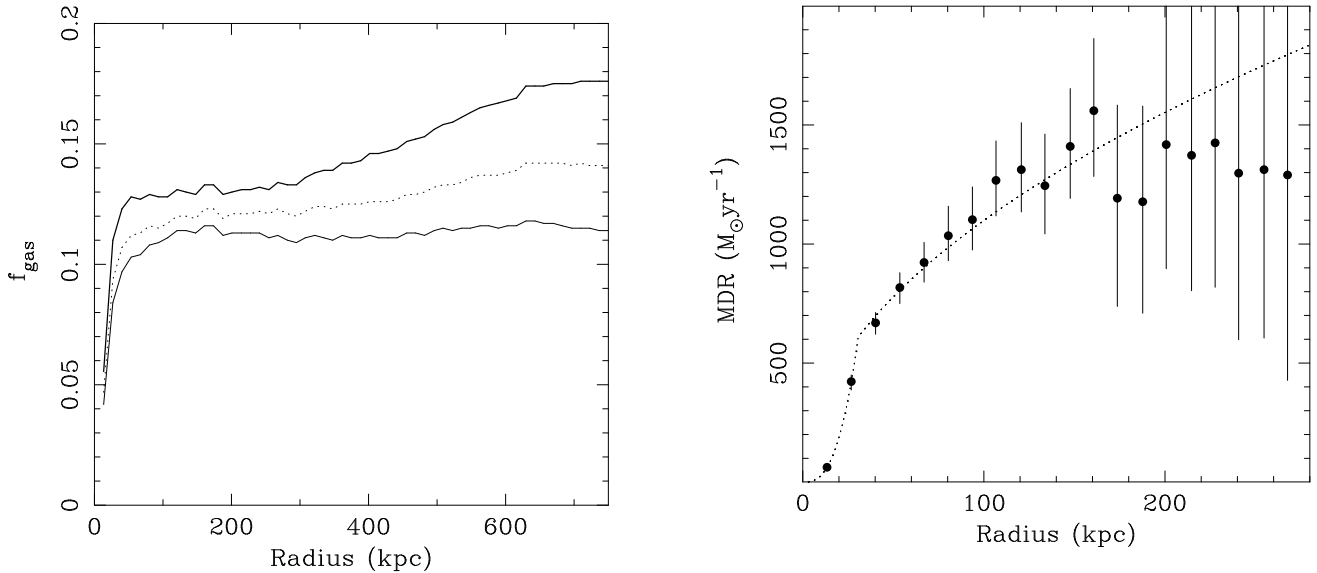


Figure 11. The ratio of the X-ray gas mass to total gravitating mass as a function of radius. The three curves show the best-fit value (dotted curve) and 1σ confidence limits (solid curves). At $r = 0.74$ Mpc we measure $f_{\text{gas}} = 0.141^{+0.035}_{-0.027}$.

for the central 100 kpc radius region is consistent with a cooling flow of $\lesssim 600 M_{\odot} \text{yr}^{-1}$, intrinsically absorbed by a column density of $1 - 4 \times 10^{21}$ atom cm^{-2} , with a mean mass-weighted flow temperature of ~ 10 keV.

Fitting the mass deposition profile in Fig. 12 with a broken power-law model, we determine a break radius of 31 ± 2 kpc, and slopes internal and external to the break radius of 2.7 ± 0.3 and 0.5 ± 0.1 , respectively (1σ errors). Allen *et al.* (2001a) argue that such breaks may mark the

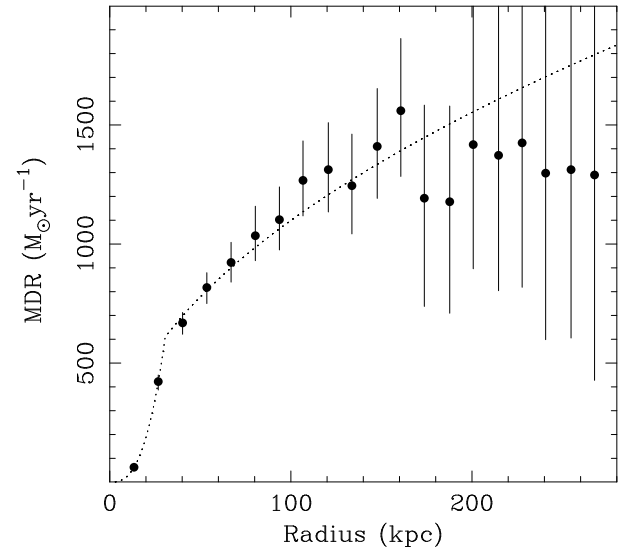


Figure 12. The mass deposition rate (MDR) determined from the image deprojection analysis under the assumption that the central regions of the cluster contain a steady-state, inhomogeneous cooling flow. Error bars are the 10 and 90 percentile values from 100 Monte Carlo simulations. The dotted line shows the best-fitting broken power-law model described in Section 7.3.

outer edges of the present-day cooling flows in clusters. The predicted MDR for the central $r \sim 20$ kpc radius, where a steady cooling flow with gas cooling to zero degrees might be expected to occur, is $\sim 200 M_{\odot} \text{yr}^{-1}$. The cooling time of the X-ray gas at the break radius is $\sim 6 \times 10^8$ yr.

8 DISCUSSION

As discussed in Section 4.2, the region of enhanced X-ray emission (and enhanced SZ effect; Komatsu *et al.* 2001) to the southeast of the main X-ray peak is significantly hotter ($kT = 18 \pm 3$ keV) than at the same distance in other directions ($kT = 12 \pm 1$ keV). Following Markevitch *et al.* (1999), we can model the properties of this region as a one-dimensional shock. In this case, the relative velocity, v , of the infalling subcluster and the shock compression factor, ρ_1/ρ_0 , can be estimated from the pre-shock (kT_0) and post-shock (kT_1) temperatures. For $kT_0 = 12$ keV and $kT_1 = 18$ keV, we obtain $v = 2250$ km s⁻¹ and $\rho_1/\rho_0 = 1.7$. If we instead adopt $kT_0 = 5$ keV, a temperature consistent with the predicted mass of the merging subcluster from the strong lensing analysis discussed in Section 6.2 (using the mass-temperature relation of Allen *et al.* 2001c), then for $kT_1 = 18$ keV we obtain $v = 4550$ km s⁻¹ and $\rho_1/\rho_0 = 3.0$. We note that the roughly spherical appearance of the shocked gas suggests that this material has expanded following the initial shock. Since the material will cool as it expands, it is likely that the initial post-shock temperature exceeded 18 keV and, for $kT_0 = 5$, that the relative collision velocity exceeded 5000 km s⁻¹. Such values are broadly consistent with the peak X-ray surface brightness enhancement of a factor ~ 3 observed at a radius of ~ 180 kpc.

The second brightest galaxy in the cluster lies approximately 18 arcsec to the east and 2 arcsec to the south of the dominant cluster galaxy. This galaxy has an extended, diffuse halo and appears to lie at the centre of a significant sub-concentration of galaxies within the cluster (Fig. 9a). These properties are consistent with it having been the dominant galaxy of the recently merged subcluster. The region of shocked X-ray gas lies approximately 11 arcsec to the south and 6.5 arcsec to the west of the second brightest galaxy. Assuming that the dark matter and galaxies associated with the subcluster have moved on ahead of the shock, it seems plausible that the subcluster travelled in from a PA of ~ 210 degrees. This is consistent with the extension of the X-ray emission observed on large scales to the south (Fig. 1b) and the weak lensing mass map presented by Fischer & Tyson (1997). Given the separation of the shocked gas and second brightest galaxy, we estimate that the shock probably occurred a few 10^7 years ago. This timescale is consistent with the spatial extent of the shocked gas, assuming that it has expanded at the sound speed, $c_s \sim 1500(T/10^8\text{K})^{-1/2}$ km s⁻¹. Note also that this timescale is comparable to the time required for the electrons and ions to reach equipartition, so it is possible that the electron and ion populations in the shocked gas have slightly different temperatures.

Despite the evidence for shocked gas in the southeast quadrant, the Chandra data for the rest of the cluster place RXJ1347.5-1145 on the $M_{2500} - kT_{2500}$ and $kT_{2500} - L_{2500}$ relations for relaxed, massive clusters discussed by Allen, Schmidt & Fabian (2001). As discussed in Section 4.4, the shocked gas produces only a small rise in the mean, emission-weighted temperature measured within the central 0.74 Mpc radius. The excess bolometric luminosity of the southeast quadrant between radii of 60-195 kpc (where the shock is most apparent) is $\sim 10^{45}$ erg s⁻¹, which corresponds to only ~ 5 per cent of the total cluster luminosity (Section 4.4). It

therefore appears that the overall temperature and luminosity of the cluster have not been boosted substantially by the merger event. This is supported by the consistent X-ray and weak lensing mass results discussed in Section 6.1.

Ricker & Sarazin (2001) and Ritchie & Thomas (2002) discuss simulations of mergers between clusters with similar central densities and argue that such mergers can lead to significant short-term increases in the overall X-ray temperatures and luminosities of clusters during the periods of closest approach. These effects are most pronounced and long-lived in clusters with relatively low central densities ($n_e \lesssim$ few 10^{-3} cm⁻³; Ritchie & Thomas 2002). The fact that large boosts in the overall temperature and luminosity are not observed in RXJ1347.5-1145 may be related to the very high central density in the main cluster core ($n_e > 10^{-1}$ cm⁻³; Fig. 10a) and could indicate that the recently-merged subcluster had a relatively low central gas density and interacted only weakly with the main cluster core.

Recently, Cohen & Kneib (2002) have published spectroscopic redshift measurements for 47 cluster members for which they determine a velocity dispersion of 910 ± 130 km s⁻¹. Inspection of their Fig. 2 suggests that a significant fraction of the galaxies with measured redshifts may have been associated with the recently merged subcluster. This could explain the relatively low velocity dispersion, in comparison to the X-ray and lensing results.

The agreement between the Chandra X-ray and gravitational lensing mass measurements for RXJ1347.5-1145 reinforces the results and conclusions drawn from previous studies of other relaxed lensing clusters *e.g.* Abell 2390 (Allen *et al.* 2001b) and Abell 1835 (Schmidt *et al.* 2001); see also the results for MS1358.4+6245 by Arabadjis *et al.* (2002). The close agreement of the independent X-ray and lensing masses indicates that the mass measurements are robust and limits the contributions from non-thermal sources of pressure support in the X-ray gas, such as bulk and/or turbulent motions and magnetic fields, in the relaxed regions of the cluster.

9 CONCLUSIONS

The main conclusions from this work may be summarized as follows:

(i) We have reported Chandra observations of RXJ1347.5-1145, the most X-ray luminous cluster of galaxies known. We have identified a region of shocked gas (enhanced X-ray brightness and temperature) to the southeast of the main X-ray peak, at a position consistent with the region of enhanced SZ effect reported by Komatsu *et al.* (2001). The shocked gas probably results from recent subcluster merger activity. The merger appears not to have boosted the overall luminosity and temperature of the cluster substantially.

(ii) Excluding the data for the southeast quadrant, we have measured the density, temperature and mass profiles for the cluster. The mass profile can be parameterized by an NFW model with a scale radius $r_s = 0.40_{-0.12}^{+0.24}$ Mpc and a concentration parameter, $c = 5.9 \pm 1.4$ (68 per cent confidence limits). The normalization of the mass profile may also be expressed in terms of an effective velocity dispersion, $\sigma = \sqrt{50}H(z)r_s c = 1450_{-200}^{+300}$ km s⁻¹.

(iii) The best-fit Chandra mass model for RXJ1347.5-1145 is in good agreement with independent measurements from weak gravitational lensing studies (Fischer & Tyson 1997). The observed strong lensing configuration in the cluster core can also be explained with the introduction of an additional mass clump centred on the second brightest galaxy, which is likely to have been the dominant galaxy of the recently merged subcluster.

ACKNOWLEDGEMENTS

We thank R. Johnstone and S. Ettori for supplying a number of scripts used in the X-ray reduction/analysis and Philippe Fischer for communicating his weak lensing results in a machine readable form. SWA and ACF acknowledge the support of the Royal Society.

REFERENCES

- Allen S.W., 1998, MNRAS, 296, 392
 Allen S.W., Fabian A.C., 1998, MNRAS, 297, L57
 Allen S.W., Ettori S., Fabian A.C., 2001b, MNRAS, 324, 877
 Allen S.W., Schmidt R.W., Fabian A.C., 2001c, MNRAS, 328, L37
 Allen S.W., Fabian A.C., Johnstone R.M., Nulsen P.E.J., Arnaud K.A., 2001a, MNRAS, 322, 589
 Anders E., Grevesse N., 1989, *Geochemica et Cosmochimica Acta* 53, 197
 Arabadjis J.S., Bautz M.W., Garmire G.P., 2002, ApJ, in press (astro-ph/0109141)
 Arnaud, K.A., 1996, in *Astronomical Data Analysis Software and Systems V*, eds. Jacoby G. and Barnes J., ASP Conf. Series volume 101, p17
 Balucinska-Church M., McCammon D., 1992, ApJ, 400, 699
 Cohen J.G., Kneib J.-P., 2002, ApJ, submitted (astro-ph/0111294)
 Dickey J.M., Lockman F.J., 1990, ARA&A, 28, 215
 Ebeling H., Rangarajan F.V.N., White D.A., 2002, MNRAS, submitted
 Ettori S., Fabian A.C., 1999, MNRAS, 305, 834
 Ettori S., Allen S.W., Fabian A.C., 2001, MNRAS, 322, 187
 Evrard A.E., 1997, MNRAS, 292, 289
 Fischer P., Tyson J.A., 1997, AJ, 114, 14
 Fukugita M., Hogan C.J., Peebles P.J.E., 1998, ApJ, 503, 518
 Jones C., Forman W., 1984, ApJ, 276, 38
 Kaastra J.S., Mewe R., 1993, *Legacy*, 3, 16, HEASARC, NASA
 Komatsu E., Kitayama T., Suto Y., Hattori M., Kawabe R., Matsuo H., Schindler S., Kohji Y., 1999, ApJ, 516, 1
 Komatsu E. *et al.*, 2001, PASJ, 53, 57
 Kriss G.A., Cioffi D.F., Canizares C.R., 1983, ApJ, 272, 439
 Liedhal D.A., Osterheld A.L., Goldstein W.H., 1995, ApJ, 438, L115
 Markevitch M., Sarazin C.L., Vikhlinin A., 1999, ApJ, 521, 526
 Moore B., Quinn T., Governato F., Stadel J., Lake G., 1999, MNRAS, 310, 1147
 Navarro J.F., Frenk C.S., White S.D.M., 1997, ApJ, 490, 493
 Nulsen P.E.J., 1998, MNRAS, 297, 1109
 O'Meara J.M., Tytler D., Kirkman D., Suzuki N., Prochaska J.X., Lubin D., Wolfe A.M., 2001, ApJ, 552, 718
 Pointecouteau E., Giard M., Benoit A., Désert F.X., Aghanim N., Coron N., Lamarre J.M., Delabrouille J., 1999, ApJL, 519, 115
 Pointecouteau E., Giard M., Benoit A., Désert F.X., Bernard J.P., Coron N., Lamarre J.M., 2001, ApJ, 552, 42
 Ricker P.M., Sarazin C.L., 2001, ApJ, 561, 621
 Ritchie B.W., Thomas P.A., 2002, MNRAS, 329, 675
 Sahu K.C. *et al.*, 1998, ApJL, 492, 125
 Schindler S. *et al.*, 1995, A&A, 299L, 9
 Schindler S., Hattori M., Neumann D.M., Böhringer H., 1997, A&A, 317, 646
 Schmidt R.W., Allen S.W., Fabian A.C., 2001, MNRAS, 327, 1057
 Schneider P., Ehlers J., Falco E.E., 1992, *Gravitational Lensing*, Springer Verlag, Berlin
 Weisskopf M.C., Tananbaum H.D., Van Speybroeck L.P., O'Dell S.L., 2000, SPIE 4012, 1 (astro-ph/0004127)
 White D.A., Fabian A.C., 1995, MNRAS, 273, 72
 White D.A., Jones C., Forman W., 1997, MNRAS, 292, 419
 White S.D.M., Frenk C.S., 1991, ApJ, 379, 52
 White S.D.M., Efstathiou G., Frenk C.S., 1993, MNRAS, 262, 1023